

Synthesis of honeycomb-shaped $\text{LiNi}_{0.5}\text{Mn}_{0.5}\text{O}_2$ using a sol-gel method with polymethylmethacrylate (PMMA) and organic surfactant

Seon-Jin Lee¹, Hea-in Kim¹, Eui-Jeong Park¹ and Jong-Tae Son^{1*}

Department of Nano-Polymer Science & Engineering, Korea National University of Transportation, Chungju, Chungbuk 27469, Republic of Korea.

Corresponding Author Email: jt1234@ut.ac.kr

<https://doi.org/10.14447/jnmes.v25i1.a04>

ABSTRACT

Received: July 15, 2021

Accepted: December 20, 2021

Keywords:

Cathode materials, Sol-gel method, PMMA, Organic surfactant, Honeycomb.

Layered-structural $\text{LiNi}_{0.5}\text{Mn}_{0.5}\text{O}_2$ has high discharge capacity, abundant availability, enhanced chemical stability, convenient environmental benignancy, and low cost. However, $\text{LiNi}_{0.5}\text{Mn}_{0.5}\text{O}_2$ suffers from poor intrinsic rate capability due to its poor ionic conductivity (2.54×10^{-7} S/cm) and poor cycle stability owing to the volume change of the cathode materials during cycling. To address this issue, honeycomb-shaped $\text{LiNi}_{0.5}\text{Mn}_{0.5}\text{O}_2$ was developed for lithium-ion batteries using a sol-gel method with spherical polymethylmethacrylate (PMMA) particles. PMMA particles provide spherical voids in $\text{LiNi}_{0.5}\text{Mn}_{0.5}\text{O}_2$ cathode materials due to their relatively low decomposition temperature (< 350 °C). Honeycomb-shaped $\text{LiNi}_{0.5}\text{Mn}_{0.5}\text{O}_2$ has a higher surface area (2.63 m²/g) than the $\text{LiNi}_{0.5}\text{Mn}_{0.5}\text{O}_2$ (2.00 m²/g) produced by conventional sol-gel method. The initial discharge capacities of conventional nano $\text{LiNi}_{0.5}\text{Mn}_{0.5}\text{O}_2$ and honeycomb-shaped $\text{LiNi}_{0.5}\text{Mn}_{0.5}\text{O}_2$ are 151.9 mAh g⁻¹ and 200.4 mAh g⁻¹, respectively at 0.1 C. After 50 cycles at 1 C, honeycomb-shaped $\text{LiNi}_{0.5}\text{Mn}_{0.5}\text{O}_2$ has a larger capacity retention than conventional nano $\text{LiNi}_{0.5}\text{Mn}_{0.5}\text{O}_2$, measuring 67.9% and 58.8% , respectively. The superior electrochemical performance of honeycomb-shaped $\text{LiNi}_{0.5}\text{Mn}_{0.5}\text{O}_2$ increases the effective surface area for Li-ion diffusion, leading to better rate capability, and buffers the volume change during Li⁺ ion insertion/extraction, improving the cycling stability.

1. INTRODUCTION

Lithium-ion batteries (LIBs) are gaining attention for their applications in Electronic vehicle (EV) [1–3]. Since $\text{LiNi}_{0.5}\text{Mn}_{0.5}\text{O}_2$ (LNMO) was first reported by Ohzuku and Makimura [4], it has been considered promising candidates for use in LIBs. The advantageous characteristics of LNMO include high discharge capacity, abundant resources, improved chemical stability, environmental benignancy, and cost competitiveness compared to LiCoO_2 [5–19]. LNMO exhibits several merits in its electrochemical performance; however, it suffers from poor intrinsic rate performance due to its poor ionic conductivity (2.54×10^{-7} S/cm [20]).

Over the past few years, some researches have sought to enhance the rate capabilities of nanostructured layer cathode materials [13–19]. Nano-sized materials exhibit higher capacities and better rate capabilities due to their shorter diffusion pathway and broader electrolyte/electrode contact areas. However, the nano-sized particles in these studies were exfoliated from the Al current collector during repeated expansion and contraction due to volume change. Therefore, it is preferable to study the surface area without reducing the particle size.

In this study, honeycomb-shaped LNMO (H-LNMO) was developed by using the sol-gel method with spherical polymethylmethacrylate (PMMA) particles and organic

surfactant. The PMMA particles provide voids in LNMO after calcination due to the lower decomposition temperatures of the particles (< 350 °C). In addition, the inner carbon layer is generated by decomposing the PMMA particles and organic surfactant during the calcining process. H-LNMO has a larger specific surface area (2.69 m²/g) than conventional nano LNMO (C-LNMO) (2.00 m²/g) because its honeycomb-shaped design generates a wide surface area without reducing the particle size to prevent exfoliation by an Al current collector [22–24]. This leads to improved ionic conductivity due to enhanced insertion and desorption of Li⁺ ions, and consequently, significantly improved discharge capacity and cycle stability compared to conventional nanoparticles.

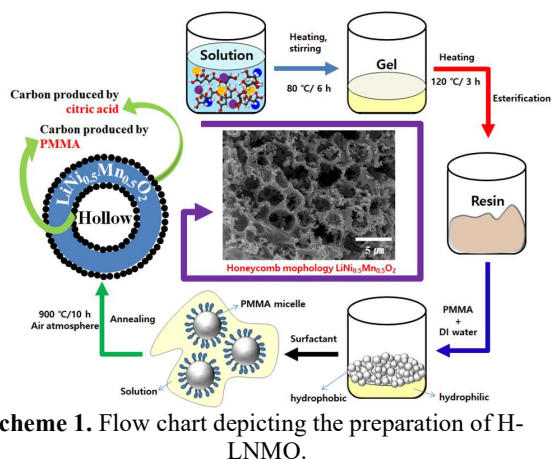
2. EXPERIMENT

2.1 Preparation of $\text{LiNi}_{0.5}\text{Mn}_{0.5}\text{O}_2$

The chemicals used for the initial steps of citrate gel synthesis were LiNO_3 : 1.379g, (Aldrich) $\text{Ni}(\text{NO}_3)_2 \cdot \text{H}_2\text{O}$: 2.907g (Aldrich), $\text{Mn}(\text{NO}_3)_2 \cdot 4\text{H}_2\text{O}$: 2.587g (Aldrich, 97%), and $\text{C}_6\text{H}_8\text{O}_7$: 7.7628g(Aldrich, 99%).

The overall procedure for the preparation of LNMO is shown in Scheme 1. The initial materials were dissolved in deionized (DI) water and stirred for 6 h at 80 °C to form a

sticky gel. The gel precursors were then dried in an oven for 3 h at 120 °C to form a resin-like sponge. The resin precursors were dissolved in DI water again, after which commercially available PMMA (ASP Corp., Korea) was added to the solution (1:1 vol. ratio). To dissolve the hydrophobic PMMA in the hydrophilic solution, polyoxyethylene (10) tridecyl ether (Aldrich) was added as a surfactant, and the solution was mixed until a paste formed. The resulting paste was calcinated at 900 °C for 10 h in open air to obtain H-LNMO.



Scheme 1. Flow chart depicting the preparation of H-LNMO.

2.2. Material characterization

X-ray diffraction (XRD) patterns for the cathodes were obtained using a Siemens D-5000 diffractometer in the 2 θ range from 10° to 80° with Cu K α radiation ($\lambda = 1.5406 \text{ \AA}$). The morphology of the powder was observed using a JSM-7610F scanning electron microscope (SEM). The particle size distribution was measured using a particle size analyzer (CILAS, 1090L).

2.3. Electrochemical test

To prepare the positive electrode, a mixture of 80%LNMO powder, 10% super-P carbon black (Sigma-Aldrich), 10% polyvinylidene difluoride (Kureha KF100) binder was added to a crucible and ground.

The resulting viscous slurry was spread on an aluminum foil using a doctor blade to achieve uniform thickness. The film was then dried at 120 °C for 4 h in a vacuum oven.

Afterwards, the CR2032-type coin cell was assembled in a glove box from the cathode film, a lithium metal foil, a porous polypropylene film, and a 1 M LiPF₆ solution in ethylene carbonate (EC)/dimethyl carbonate (DMC) mixture (volume ratio = 3:7).

Lithium metal foil was used as the counter and reference electrodes, respectively. After the coin cell assembly, the test cells were charged and discharged galvanostatically between 3.0 and 4.6 V versus Li/Li⁺ at a constant current density (17 mA g⁻¹ at a rate of 0.1 C). Cycle performances were carried out at a high current density (170 mA g⁻¹ at a rate of 1 C rate). Volume of electrolyte: 0.2ml, Ar atmosphere, glove box brand :korea kiyon , glove box moisture content: 0.4ppm.

3. RESULTS AND DISCUSSION

Figure 1 (a) shows an SEM image of the as-prepared C-LNMO. The average particle size of C-LNMO was estimated

to be 100–300 nm. The PMMA decomposition process at a temperature of 200 °C (Figure 1 (b)) shows that the honeycomb structure of H-LNMO is formed by evaporation before reaching the synthesis temperature. The average diameter of PMMA measured by PSA was approximately 5 μm . The pore diameters within the LNMO were 4.12 μm on average, similar to the particle size of PMMA. Figure 1(e) shows the average particle size of honeycomb-shaped LiNi_{0.5}Mn_{0.5}O₂. The average size is 21.42 μm . Figure 1 (f) there is no carbon peak of PMMA. It is considered that the carbon peak is not observed because PMMA is an amorphous material.

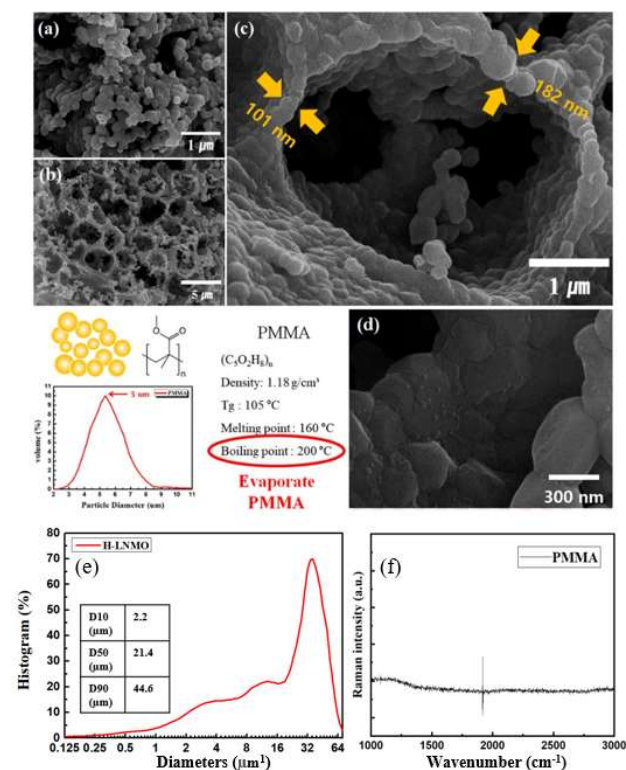


Figure 1. SEM images of (a) conventional nano (C-LNMO) and (b) honeycomb-shaped LiNi_{0.5}Mn_{0.5}O₂ (H-LNMO) materials. (Inset (c) is an expanded image of (b), and inset (d) is an expanded image of (c)). (e) PSA images of honeycomb-shaped LiNi_{0.5}Mn_{0.5}O₂ (f) Raman spectra of PMMA in 1000-3000 cm⁻¹

This result suggests that the solid-state diffusion length of Li⁺ in H-LNMO is shorter than that of Li⁺ in C-LNMO. These factors indicate that H-LNMO has significantly improved rate performance compared to C-LNMO.

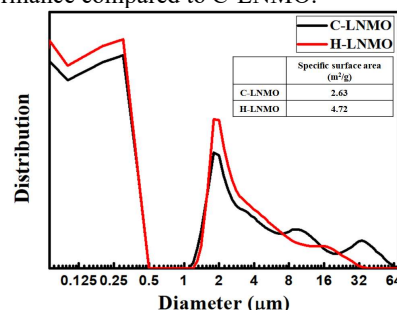


Figure 2. Particle size distributions and specific surface areas of C-LNMO and H-LNMO.

The particle size distribution of the as-synthesized C-LNMO and H-LNMO samples was measured by PSA, shown in Figure 2. The primary particles were nano-sized. However, the secondary particles were agglomerated and ranged in size from 1.1 to 64 μm . H-LNMO had smaller aggregated particle sizes than C-LNMO due to CO_2 and O_2 gas generated by the evaporation of PMMA. The gases can physically block particle agglomeration. The specific surface area was also measured. H-LNMO had a larger specific surface area (4.72 m^2/g) than C-LNMO (2.63 m^2/g) due to the reduction in aggregated secondary particle size and the shape of the pores, as shown in the SEM images.

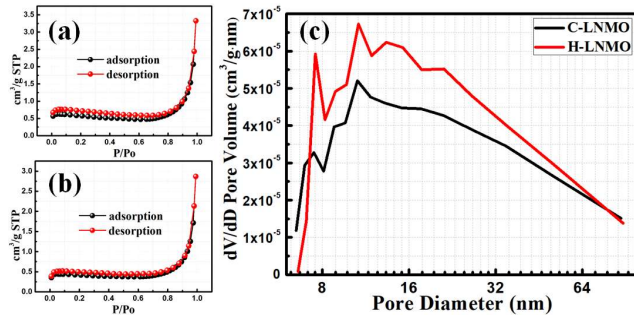


Figure 3. Nitrogen adsorption and desorption isotherms for (a) C-LNMO and (b) H-LNMO, and (c) the corresponding pore size distribution curve determined.

The Brunauer–Emmett–Teller (BET) specific surface areas of C-LNMO and H-LNMO were measured using N_2 adsorption–desorption isotherms at 77K (Figure 3 (a) and (b)). Notably, C-LNMO had a BET surface area of 2.00 m^2g^{-1} , which was much smaller than that of H-LNMO (2.69 m^2g^{-1}).

In addition, the pore-size distribution analysis shown in Figure 3(c) indicated that H-LNMO possessed a relatively larger pore size distribution. These results showed that spherical PMMA can inhibit the aggregation of nanoparticles and dramatically increase the surface area.

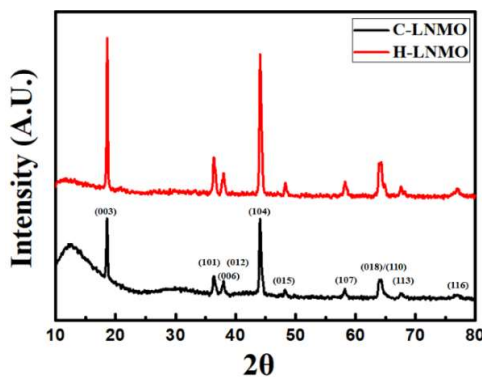


Figure 4. (a) XRD patterns of C-LNMO and H-LNMO cathode materials. (b)

Table 1. Lattice parameters of C-LNMO and H-LNMO

| Sample | a (Å) | c (Å) | Volume (Å ³) |
|--------|-----------------|------------------|--------------------------|
| C-LNMO | 2.895 (± 0.004) | 14.166 (± 0.013) | 102.778 |
| H-LNMO | 2.895 (± 0.003) | 14.142 (± 0.009) | 102.634 |

Figure 4. shows the XRD patterns of the as-synthesized C-LNMO and H-LNMO samples. The diffraction peaks of both C-LNMO and H-LNMO indicated a pristine hexagonal structure with an R3m space group. With the same synthetic solution, a fairly broad peak was observed around 13° for C-LNMO, whereas a weak peak was observed in the same location for H-LNMO. It is speculated that the difference in peak strengths occurs due to O_2 gas produced by the evaporation of PMMA reacting with the carbon residue. As a result, the thickness of the carbon coating can be controlled by varying the volume of PMMA.

Table 1 lists the lattice parameters of the C-LNMO and H-LNMO samples. Although H-LNMO had a larger surface area than C-LNMO, there was no significant change in the size of the lattice parameters.

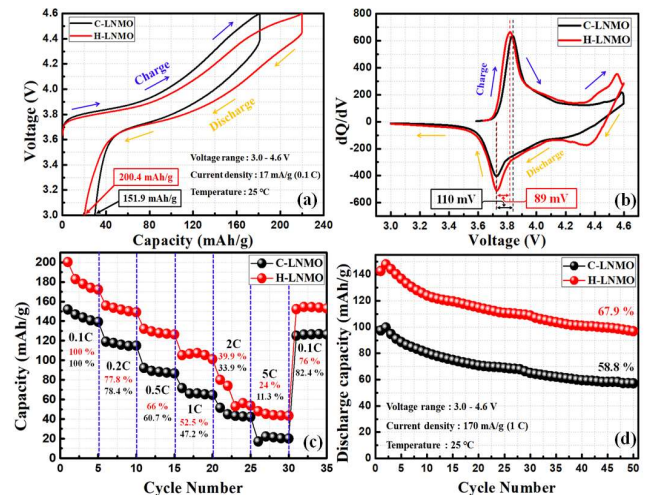


Figure 5. (a) Initial charge–discharge curves and (b) differential capacity versus voltage plots of C-LNMO and H-LNMO in the voltage range 3.0–4.6 V at 0.1 C. (c) Rate capabilities of C-LNMO and H-LNMO. (d) Discharge capacity versus cycle number of C-LNMO and H-LNMO cycled at 1 C in the voltage range 3.0–4.6 V at 25 °C.

As shown in Figure 5 (a), the initial charge–discharge capacities of C-LNMO and H-LNMO were evaluated between 3.0 and 4.6 V at a constant current density of 17 mAg^{-1} (rate of 0.1 C) and a temperature of 25 °C. The initial discharge capacities of C-LNMO and H-LNMO were 151.9 mAhg^{-1} and 200.4 mAhg^{-1} , respectively. The differential capacity versus voltage plot (Figure 5 (b)) illustrates the polarization between the charge–discharge peaks of C-LNMO and H-LNMO, at 89 mV and 110 mV, respectively.

Figure 5 (c) shows the rate capabilities of C-LNMO and H-LNMO. The rate performance of H-LNMO was higher than that of C-LNMO for all C-rate ranges. Figure 5 (d) shows the discharge capacities versus cycle number of C-LNMO and H-LNMO when the materials were evaluated in the voltage range 3.0–4.6 V at a constant current density of 170 mAg^{-1} (rate of 1 C) and a temperature of 25 °C.

After 50 cycles, the remaining capacity of H-LNMO (67.9%) was higher than that of C-LNMO (57.8%). These results suggest that smaller grains in the composite shorten the diffusion length of Li^+ , and macro-pores and a wide specific surface

area improve the interfacial contact between the electrode and electrolyte [25].

In addition, the enhanced cycle stability suggests that the structure of H-LNMO induces volume expansion and contraction to the inner cavities during cycling, thereby preventing the exfoliation of the electrode from the Al current collector. This shows improved ionic conductivity due to enhanced insertion and desorption of Li^+ ions, and consequently, significantly improved electrochemical performance compared to conventional nanoparticles.

Table 2. Film resistance of the surface membrane (R_{SEI}) and charge-transfer resistance (R_{ct}) of C-LNMO and H-LNMO by Nyquist circles

| Sample | R_{SEI} (Ω) (before cell test) | R_{ct} (Ω) (before cell test) | R_{SEI} (Ω) (after 50 cycles) | R_{ct} (Ω) (after 50 cycles) |
|--------|---|--|--|---|
| C-LNMO | 76.05 | 254.62 | 71.36 | 599.62 |
| H-LNMO | 32.33 | 299.88 | 8.12 | 11.86 |

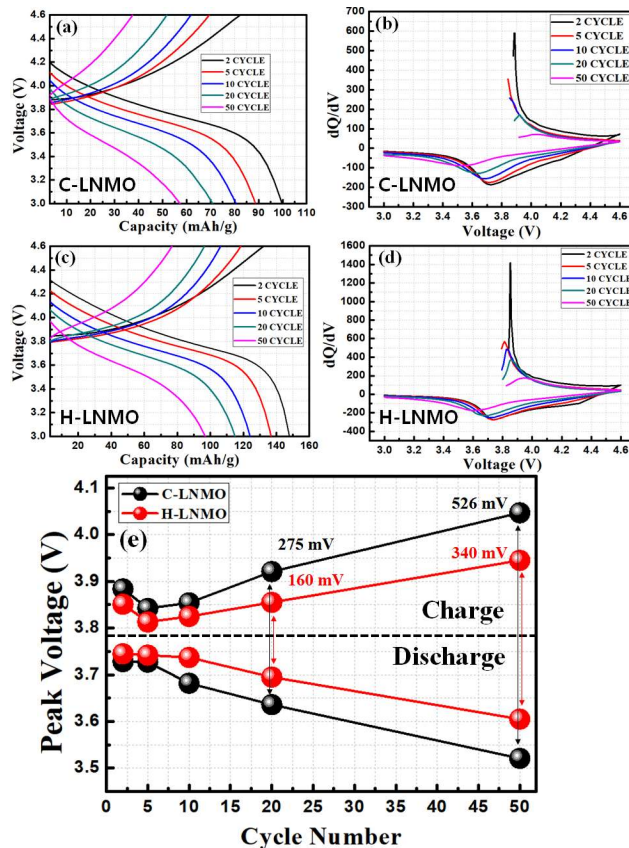


Figure 6. (a), (c) Initial charge–discharge curves and (b), (d) differential capacity versus voltage plots of C-LNMO and H-LNMO in the voltage range from 3.0 to 4.6 V at 1 C. (e) Peak voltage of differential capacity plots versus cycle number.

Figure 6 illustrates various behaviors that confirm the benefits of increased surface area. Figure 6 (a) and (c) depict initial charge–discharge curves and Figure 6 (b) and 6 (d) show differential capacity patterns versus voltage from 3.0 to 4.6 V at 1 C.

Figure 6 (e) illustrates the peak voltages of the differential capacity plots versus cycle number. In both samples, the overvoltage increases as the cycles progress; however, the overvoltage of H-LNMO is noticeably less than that of C-LNMO.

The overvoltages at 20 cycles were 275 mV and 160 mV for C-LNMO and H-LNMO, respectively, and the overvoltages at 50 cycles were 526 mV and 340 mV, respectively. The differences between the overvoltages of C-LNMO and H-LNMO in cycles 20 and 50 were 115mV and 186mV, respectively. This result is evidence that the honeycomb-shaped structure facilitates the diffusion of Li^+ as the cycles progress.

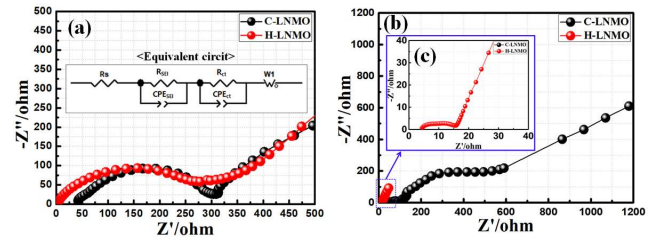


Figure 7. Impedance plot of C-LNMO and H-LNMO electrodes (a) before the cell test and (b) after 50 cycles at the state of charge = 0. (c) Inset figure displaying the enlarged Nyquist circles at higher frequencies.

Figure 7 shows the AC impedance spectrum and Nyquist plot which demonstrate the improved electrochemical performance of the half-cell. The impedance results were interpreted using an equivalent circuit.

In Figure 7 (a), R_s is the ohmic resistance of the electrolyte solution, R_{SEI} is the film resistance of the surface membrane, and R_{ct} is the charge-transfer resistance at the electrolyte [26,27].

Figure 7 (a) shows the Nyquist plot before the cell test. The R_{SEI} values of C-LNMO and H-LNMO were 76.05 Ω and 32.33 Ω , respectively, and the R_{ct} values were 254.62 Ω and 299.88 Ω , respectively. These results are listed in Table 2. The R_{ct} increased because the large surface area of H-LNMO helps the sufficient penetration of the electrolyte.

Figure 7 (b) shows the Nyquist plot after 50 cycles. The R_{SEI} values of C-LNMO and H-LNMO were 71.36 Ω and 8.12 Ω , respectively, and the R_{ct} values were 599.62 Ω and 11.86 Ω , respectively, as shown in Table 2. The reason for the drastic decrease in R_{ct} was due to the increased number of Li^+ diffusion paths resulting from the large surface area of H-LNMO.

4. CONCLUSION

H-LNMO was successfully synthesized using a sol-gel method with PMMA and an organic surfactant. The XRD results indicated an α - NaFeO_2 structure. The primary particle sizes of C-LNMO were approximately 100–300 nm. The wall thickness of H-LNMO was approximately 142 nm. The specific surface areas of the as-synthesized C-LNMO and H-LNMO samples were 2.00 m^2g^{-1} and 2.69 m^2g^{-1} , respectively. The initial discharge capacities of C-LNMO and H-LNMO were 151.9 m^2g^{-1} and 200.4 m^2g^{-1} , respectively. The rate performance of H-LNMO was higher than that of C-LNMO for all C-rate ranges. The large specific surface area and the

short Li^+ diffusion pathways of H-LNMO increased ionic conductivity due to enhanced insertion and desorption of Li^+ ions and improved the discharge capacity and rate performance of the material compared to conventional nanoparticles.

ACKNOWLEDGMENT

Financial support for this study was granted by the Ministry of SMEs and Startups, the Republic of Korea (S2928638), and the National Research Foundation of Korea (NRF), which is funded by the Korean government (MSIT) (No. 2021R1F1A1063481). Additional financial support was provided by the Technology Innovation Program (or Industrial Strategic Technology Development Program-Material Parts Technology Development Project) (20003747, Development of high-performance cathode material manufacturing technology through valuable metal upcycling from waste battery and waste cathode material), which is funded by the Ministry of Trade, Industry & Energy (MOTIE, Korea).

REFERENCES

- [1] Balke, N., Jesse, S., Morozovska, A., Eliseev, E., Chung, D., Kim, Y., Adamczyk, L., García, R., Dudney, N. and S., Kalinin. (2010). Nanoscale mapping of ion diffusion in a lithium-ion battery cathode. *Nature Nanotechnology*, 5(10): 749-754.
- [2] Kim, S., Yun, J., Son, B., Lee, Y., Kim, K., Lee, Y., Cho, K. (2014). Graphite/silicon hybrid electrodes using a 3D current collector for flexible batteries. *Advanced Materials*, 26(19): 2977-2982.
- [3] Wang, M., Li, X., Gao, M., Pan, H., Liu, Y. (2014). A Novel synthesis of MgS and its application as electrode material for lithium-ion batteries. *Journal of Alloys and Compounds*, 603: 158-166.
- [4] Wu, Y., Gao, M., Li, X., Liu, Y., Pan, H. (2014). Preparation of mesohollow and microporous carbon nanofiber and its application in cathode material for lithium-sulfur batteries. *Journal of Alloys and Compounds*, 608: 220-228.
- [5] Gu, Y., Chen, Y., Liu, H., Wang, Y., Wang, C., Wu, H. (2011). Structural characterization of layered $\text{LiNi}_{0.85-x}\text{Mn}_x\text{Co}_{0.15}\text{O}_2$ with $x=0, 0.1, 0.2$ and 0.4 oxide electrodes for Li batteries., *Journal of Alloys and Compounds*, 509(30): 7915-7921.
- [6] Islam, M., Davies, R., Gale, J. (2003). Structural and electronic properties of the layered $\text{LiNi}_{0.5}\text{Mn}_{0.5}\text{O}_2$ lithium battery material. *Chemistry of Materials*, 15(22): 4280-4286.
- [7] Fergus, J. (2010). Recent developments in cathode materials for lithium ion batteries. *Journal of Power Sources*, 195(4): 939-954.
- [8] Li, D., Yuan, C., Dong, J., Peng, Z., Zhou, Y. (2007). Synthesis and electrochemical properties of $\text{LiNi}_{0.85-x}\text{Co}_x\text{Mn}_{0.15}\text{O}_2$ as cathode materials for lithium-ion batteries. *Journal of Solid State Electrochemistry*, 12(3): 323-327.
- [9] Gao, D., Li, Y., Lai, X., Bi, J., Lin, D. (2011). Room-temperature synthesis of crystallized LiCoO_2 thin films by electrochemical technique. *Journal of Alloys and Compounds*, 509(3): 697-703.
- [10] Ohzuku, T., Makimura, Y. (2001). Layered lithium insertion material of $\text{LiNi}_{1/2}\text{Mn}_{1/2}\text{O}_2$: a possible alternative to LiCoO_2 for advanced lithium-ion batteries. *Chemistry Letters*, 30(8): 744-745
- [11] Ahn, W., Lim, S., Jung, K., Yeon, S., Kim, K., Song, H., Shin, K. (2014). Combustion-synthesized $\text{LiNi}_{0.6}\text{Mn}_{0.2}\text{Co}_{0.2}\text{O}_2$ as cathode material for lithium ion batteries. *Journal of Alloys and Compounds*, 609: 143-149.
- [12] Lu, Y., Jiang, Y., Yang, Z., Han, J., Huang, Y. (2013). Ma, J. Polymer-assisted synthesis of $\text{LiNi}_{2/3}\text{Mn}_{1/3}\text{O}_2$ cathode material with enhanced electrochemical performance. *Journal of Alloys and Compounds*, 559: 203-208.
- [13] Hwang, B., Yu, T., Cheng, M., Santhanam, R. (2009). Rapid microwave-enhanced ion exchange process for the synthesis of $\text{LiNi}_{0.5}\text{Mn}_{0.5}\text{O}_2$ and its characterization as the cathode material for lithium batteries. *Journal of Materials Chemistry*, 19(26): 4536-4544.
- [14] Liu, Y., Chen, B., Cao, F., Zhao, X., Yuan, J. (2011). Synthesis of nano architected $\text{LiNi}_{0.5}\text{Mn}_{0.5}\text{O}_2$ spheres for high-performance rechargeable lithium-ion batteries via an in situ conversion route. *Journal of Materials Chemistry*, 21(28): 10437-10441.
- [15] Lu, X., Sun, Y., Jian, Z., He, X., Gu, L., Hu, Y., Li, H., Wang, Z., Chen, W., Duan, X., Chen, L., Maier, J., Tsukimoto, S., Ikuhara, Y. (2012). New insight into the atomic structure of electrochemically delithiated $\text{O}_3\text{-Li}_{(1-x)}\text{CoO}_2$ ($0 \leq x \leq 0.5$) nanoparticles. *Nano Letters*, 12(12): 6192-6197.
- [16] Shannon, R. (1976). Revised effective ionic radii and systematic studies of interatomic distances in halides and chalcogenides. *Acta Crystallographica Section A*, 32(5): 751-767.
- [17] Reimers, J. (1992). Electrochemical and in situ X-Ray diffraction studies of lithium intercalation in Li_xCoO_2 . *Journal of The Electrochemical Society*, 139(8): 2091-2097.
- [18] Amatucci, G. (1996). CoO_2 , The end member of the Li_xCoO_2 solid solution. *Journal of The Electrochemical Society*, 143(3): 1114-1123.
- [19] Li, H., Yabuuchi, N., Meng, Y., Kumar, S., Breger, J., Grey, C., Shao-Horn, Y. (2007). Changes in the cation ordering of layered O_3 $\text{Li}_x\text{Ni}_{0.5}\text{Mn}_{0.5}\text{O}_2$ during electrochemical cycling to high voltages: an electron diffraction study. *Chemistry of Materials*, 19(10): 2551-2565.
- [20] Xia, H., Tang, S., Lu, L. (2008). Novel synthesis and electrochemical behavior of layered $\text{LiNi}_{0.5}\text{Mn}_{0.5}\text{O}_2$. *Journal of Alloys and Compounds*, 449(1-2): 296-299.
- [21] Meng, X., Dou, S., Wang, W. High power and high capacity cathode material $\text{LiNi}_{0.5}\text{Mn}_{0.5}\text{O}_2$ for advanced lithium-ion batteries. *Journal of Power Sources*, 184(2): 489-493.
- [22] Zhang, X., Jiang, W., Mauger, A., Qilu, Gendron, F., Julien, C. (2010). Minimization of the cation mixing in $\text{Li}_{1+x}(\text{NMC})_{1-x}\text{O}_2$ as cathode material. *Journal of Power Sources*, 195(5): 1292-1301.
- [23] Song, M., Park, C., Park, H., Mumm, D. (2012). Variations in the electrochemical properties of metallic elements-substituted LiNiO_2 cathodes with preparation

- and cathode fabrication conditions. *Electronic Materials Letters*, 8(1): 37-42.
- [24] Song, M., Park, C., Yoon, S., Park, H., Mumm, D. The effects of C-rate on the discharge capacities of $\text{LiNi}_{1-y}\text{M}_y\text{O}_2$ (M=Ni, Ga, Al and/or Ti) cathodes. *Electronic Materials Letters*, 5(4), 151-155: (2009).
- [25] Lee, K., Myung, S., Prakash, J., Yashiro, H., Sun, Y. (2008). Optimization of microwave synthesis of $\text{Li}[\text{Ni}_{0.4}\text{Co}_{0.2}\text{Mn}_{0.4}]\text{O}_2$ as a positive electrode material for lithium batteries. *Electrochimica Acta*, 53(7): 3065-3074.
- [26] Cai, L., Liu, Z., An, K., Liang, C. (2012). Probing Li-Ni cation disorder in $\text{Li}_{1-x}\text{Ni}_{1+x-y}\text{Al}_y\text{O}_2$ cathode materials by neutron diffraction. *Journal of The Electrochemical Society*, 159(7): A924-A928.
- [27] Stoyanova, R. (2000). Aluminium coordination in $\text{LiNi}_{1-y}\text{Al}_y\text{O}_2$ solid solutions. *Solid State Ionics*, 128(1-4): 1-10.

NOMENCLATURE

| | |
|--------------------|-------------|
| $^{\circ}\text{C}$ | temperature |
| g | weight |
| V | Voltage |

Greek symbols

| | |
|-----------|------------------------|
| λ | wavelength |
| θ | angle |
| μ | Micro- (one millionth) |